Enhancement of Interdecadal Climate Variability in the Sahel by Vegetation Interaction

Ning Zeng, *et al.*

Science **286**, 1537 (1999);
DOI: 10.1126/science.286.5444.1537

Science (print ISSN 0036-8075; online ISSN 1095-9203) is published weekly, except the last week in December, by the American Association for the Advancement of Science, 1200 New York Avenue NW, Washington, DC 20005.

Sayan Ranges, and Tian Shan, which skirt the border regions of Russia, Mongolia, China, and Kazakhstan (Fig. 4E). These mountain waves are present at all heights, reaching the uppermost levels of the stratosphere (Fig. 4C). There is also evidence of more isolated mountain wave activity over the Alps and the Alaska-Yukon region. Mountain waves are largely absent in both the observations and model results over other mountainous regions, such as western North America, the Himalayas, Greenland, and Scandinavia. This absence occurs in the MWFM results because regional winds inhibit mountain wave propagation into the stratosphere.

Despite the basic similarities, specific differences between the CRISTA data and MWFM results are also evident in Figs. 3 and 4. Shortcomings in the model may be implicated here, highlighting the potential value of observations such as these in improving global mountain wave parameterizations.

Figure 4C also shows large $\hat{T}$ amplitudes at $z = 45$ km at the northernmost latitudes, which cannot be explained in terms of polar mountain waves (Fig. 4F). This observation is consistent with large gravity-wave amplitudes observed previously in ground-based soundings of the high-latitude winter upper stratosphere (*28*). The feature has been attributed to enhanced $\exp(z/2H_\rho)$ amplitude growth of weaker "background" gravity-wave activity, due to the temperature structure of the winter polar stratosphere (*13*, *29*), although longitudinal asymmetries in stratospheric winds can modulate the effect substantially (*30*). This indicates that CRISTA measured gravity waves from sources other than mountains as well.

References and Notes

1. R. B. Smith, *Adv. Geophys.* **21**, 87 (1979); M. G. Wurtele, R. D. Sharman, A. Datta, *Annu. Rev. Fluid Mech.* **28**, 429 (1996).
2. T. N. Palmer, G. J. Shutts, R. Swinbank, *Q. J. R. Meteorol. Soc.* **112**, 1001 (1986); N. McFarlane, *J. Atmos. Sci.* **44**, 175 (1987); J. Zhou, Y. C. Sud, K.-M. Lau, *Q. J. R. Meteorol. Soc.* **122**, 903 (1996).
3. D. K. Lilly and P. F. Lester, *J. Atmos. Sci.* **31**, 800 (1974).
4. J. T. Bacmeister, P. A. Newman, B. L. Gary, K. R. Chan, *Weather Forecasting* **9**, 241 (1994).
5. F. M. Ralph, P. J. Nieman, D. Levinson, *Geophys. Res. Lett.* **24**, 663 (1997); R. M. Worthington, *J. Atmos. Sol.-Terr. Phys.* **60**, 1543 (1998).
6. J.-F. Lamarque, A. O. Langford, M. H. Proffitt, *J. Geophys. Res.* **101**, 22969 (1996); T. Schilling, F.-J. Lübken, F. G. Wienhold, P. Hoor, H. Fischer, *Geophys. Res. Lett.* **26**, 303 (1999).
7. D. Cariolle, S. Muller, F. Cayla, M. P. McCormick, *J. Geophys. Res.* **94**, 11233 (1989); T. Deshler, T. Peter, R. Müller, P. Crutzen, *Geophys. Res. Lett.* **21**, 1327 (1994); K. S. Carslaw *et al.*, *J. Geophys. Res.* **103**, 5785 (1998); K. S. Carslaw, T. Peter, J. T. Bacmeister, S. D. Eckermann, *J. Geophys. Res.* **104**, 1827 (1999); J. Schreiner *et al.*, *Science* **283**, 968 (1999).
8. K. S. Carslaw *et al.*, *Nature* **391**, 675 (1998).
9. K. Sato, *J. Atmos. Sci.* **47**, 2803 (1990); F. M. Ralph, M. Crochet, S. V. Venkateswaran, *Q. J. R. Meteorol. Soc.* **118**, 597 (1992); R. M. Worthington and L. Thomas, *Geophys. Res. Lett.* **24**, 1071 (1997); C. M. Scavuzzo, M. A. Lamfri, H. Teitelbaum, F. Lott, *J. Geophys. Res.* **103**, 1747 (1998); J. A. Whiteway, *J. Atmos. Sci.* **56**, 1344 (1999).
10. G. J. Shutts and A. Broad, *Q. J. R. Meteorol. Soc.* **119**, 377 (1993); J. L. Attié, A. Druilhet, P. Durand, B. Bénech, *Ann Geophys.* **15**, 823 (1997); J. Dean-Day *et al.*, *Geophys. Res. Lett.* **25**, 1351 (1998).
11. J. T. Bacmeister, M. R. Schoeberl, L. R. Lait, P. A. Newman, B. Gary, *Geophys. Res. Lett.* **17**, 81 (1990); G. D. Nastrom and D. C. Fritts, *J. Atmos. Sci.* **49**, 101 (1992).
12. E. J. Fetzer and J. C. Gille, *J. Atmos. Sci.* **51**, 2461 (1994); D. L. Wu and J. W. Waters, *Geophys. Res. Lett.* **23**, 3631 (1996); R. H. Picard *et al.*, *Geophys. Res. Lett.* **25**, 2809 (1998).
13. M. J. Alexander, *J. Geophys. Res.* **103**, 8627 (1998).
14. D. Offermann *et al.*, *J. Geophys. Res.* **104**, 16311 (1999). CRISTA-SPAS orbited ~100 km behind the shuttle, with the CRISTA telescopes pointed opposite to the orbital motion (backward viewing). The left and right telescopes scanned the limb 18° on either side of the center telescope. This corresponds to tangent heights separated by ~600 km.
15. M. Riese *et al.*, *J. Geophys. Res.* **104**, 16349 (1999).
16. Riese *et al.* (*15*) give full details of version 1 CRISTA retrievals, which yielded temperatures of ~1 K precision. Data analyzed here come from improved version 2 retrievals (precision of ~0.5 K).
17. P. Preusse, B. Schaeler, J. T. Bacmeister, D. Offermann, *Adv. Space Res.*, in press. Visibility is defined here as the measured wave temperature amplitude divided by its actual amplitude.
18. There were two main measurement modes: a stratosphere mode (77 hours of data every 200 km along track) and a stratosphere-mesosphere mode (55 hours of data every 400 km along track). Additionally, every fourth profile was a high-altitude scan (HAS) (*15*). HAS data were not analyzed here.
19. See, for example, section 2.1 of D. C. Fritts, *Rev. Geophys.* **22**, 275 (1984).
20. EP flux F is conserved for a nonbreaking, steady plane mountain wave [A. Eliassen and E. Palm, *Geofys. Publ.* **22**, 1 (1961)]. With the use of irrotational hydrostatic gravity-wave relations, it can be evaluated from measured mountain wave variables as

$$F = \frac{-\rho g \lambda_z \hat{T}^2}{2\bar{T}\lambda_h[d\bar{T}/dz + \Gamma_a]}$$

where ρ is atmospheric density and g is gravitational acceleration. This equation yields a predominantly westward EP flux ~0.02 to 0.2 Pa below 30 km (given the quoted uncertainties in λ_h and $\hat{T}$). When mountain waves break, the vertical EP flux gradient quantifies the force exerted on the atmosphere and the intensity of turbulence generated locally (*2*, *4*, *19*, *22*).
21. M. J. Alexander and K. Rosenlof, *J. Geophys. Res.* **101**, 23465 (1996).
22. An improved research version of MWFM was used here, which uses ray-tracing methods to better simulate the amplitudes and three-dimensional nonhydrostatic propagation of waves through the atmosphere [S. D. Eckermann and C. J. Marks, *Adv. Space Res.* **20** (no. 6), 1253 (1997)].
23. L. Coy and R. Swinbank, *J. Geophys. Res.* **102**, 25763 (1997).
24. M. Leutbecher and H. Volkert, *Geophys. Res. Lett.* **23**, 3329 (1996); A. Dörnbrack, M. Leutbecher, H. Volkert, M. Wirth, *Meteorol. Appl.* **5**, 117 (1998).
25. CRISTA ozone and trace gas data show this clearly; see Plate 2a of M. Riese *et al.* [*J. Geophys. Res.* **104**, 16349 (1999)] and Plate 5 of M. Riese, X. Tie, G. Brasseur, and D. Offermann [*J. Geophys. Res.* **104**, 16419 (1999)].
26. R. R. Garcia and B. A. Boville, *J. Atmos. Sci.* **51**, 2238 (1994); T. J. Duck, J. A. Whiteway, A. I. Carswell, *Geophys. Res. Lett.* **25**, 2813 (1998).
27. There are a number of reasons for these differences. Although efforts were made to correct for observational smearing of the CRISTA $\hat{T}$ values, measured amplitudes may still be substantially underestimated. Additionally, linear plane-wave parameterizations such as MWFM tend to overestimate wave amplitudes [S. A. Smith, D. C. Fritts, T. E. VanZandt, *J. Atmos. Sci.* **44**, 1404 (1987); G. J. Shutts, *Q. J. R. Meteorol. Soc.* **124**, 1421 (1998)].
28. I. Hirota, *J. Atmos. Terr. Phys.* **46**, 767 (1984); S. D. Eckermann, I. Hirota, W. K. Hocking, *Q. J. R. Meteorol. Soc.* **121**, 149 (1995).
29. S. D. Eckermann, *J. Atmos. Terr. Phys.* **57**, 105 (1995).
30. J. A. Whiteway *et al.*, *Geophys. Res. Lett.* **24**, 1387 (1997).

31. This research was supported by the Office of Naval Research and by NASA through the Atmospheric Chemistry Modeling and Analysis Program and the Upper Atmosphere Research Satellite Guest Investigator Program.

17 June 1999; accepted 19 October 1999

Enhancement of Interdecadal Climate Variability in the Sahel by Vegetation Interaction

Ning Zeng,[1]* J. David Neelin,[1] K.-M. Lau,[2] Compton J. Tucker[2]

The role of naturally varying vegetation in influencing the climate variability in the West African Sahel is explored in a coupled atmosphere–land-vegetation model. The Sahel rainfall variability is influenced by sea-surface temperature variations in the oceans. Land-surface feedback is found to increase this variability both on interannual and interdecadal time scales. Interactive vegetation enhances the interdecadal variation substantially but can reduce year-to-year variability because of a phase lag introduced by the relatively slow vegetation adjustment time. Variations in vegetation accompany the changes in rainfall, in particular the multidecadal drying trend from the 1950s to the 1980s.

The rainfall over the West African Sahel region (*1*) shows a multidecadal drying trend from the 1950s to the 1980s and early 1990s, as well as strong interannual variability (Fig. 1A). Causes proposed to explain this dramatic trend include global sea surface temperature (SST) variations (*2–5*) and land use change, that is, the desertification process (*6, 7*). Because vegetation distribution tends to be controlled largely by climate (*8, 9*), and surface property changes can affect climate by modifying the atmospheric energy and water budget (*10–13*), it is reasonable to propose that dynamic vegetation-climate interaction might influence decadal climate variability substantially in a climatically sensitive zone such as the Sahel. We tested this

hypothesis in a coupled atmosphere–land-vegetation model of intermediate complexity.

The atmospheric component of the model is the Quasi-equilibrium Tropical Circulation Model (QTCM) (*14, 15*), which is coupled to the land surface model Simple-Land (SLand) (*15*). The QTCM simulates a seasonal climate over the Sahel that is close to observations and that compares favorably with current atmospheric general circulation models (GCMs). We modeled the major effects of a varying vegetation on climate through its control of the evapotranspiration process and modification of surface albedo with SLand. Other effects, such as surface roughness and modification of soil properties, were not considered.

Vegetation growth in the tropics responds mostly to the interannual variations of water availability and is less influenced by temperature and nutrient limitation on these time scales because of the relatively large rainfall variability there. The central equation in the dynamic vegetation model is a biomass equation driven by photosynthesis and vegetation loss

$$\frac{dV}{dt} = a\beta(w)(1 - e^{-kL}) - V/\tau \qquad (1)$$

where t is time, a is a carbon assimilation coefficient, β is the soil moisture dependence as used in the original SLand, w is soil wetness, L is the plant leaf area index (LAI), and k is the extinction coefficient of photosynthetically active sunlight taken as 0.75. The vegetation time scale τ is set to 1 year. This equation is similar to the biomass equations used in models with more explicit vegetation dynamics (*16–19*). V is interpreted as vegetation amount or leaf biomass, and it is normalized between 0 and 1. The LAI is assumed to be directly proportional to V as $L = L_{max}V$, where L_{max} is a maximum LAI of 8. The carbon assimilation coefficient a takes a value such that $V = 1$ at equilibrium ($dV/dt = 0$) and without water stress ($\beta = 1$). This model does not explicitly include plant competition nor does it consider species-specific characteristics such as resource allocation. Seasonality is not explicitly modeled for V, so Eq. 1 represents variation on the background of a mean seasonal cycle.

The original version of the land model was modified to account for the effects of leaf-to-canopy scaling (*20*) so that the canopy conductance g_c for evapotranspiration is

$$g_c = g_{s_{max}}\beta(w)(1 - e^{-kL})/k \qquad (2)$$

where $g_{s_{max}}$ is a leaf-level maximum conductance. Note that photosynthesis and evapotranspiration are closely related in Eqs. 1 and 2 (*20*). Besides modifying evapotranspiration through Eq. 2, vegetation also changes land surface albedo A as (*21*)

$$A = 0.38 - 0.3(1 - e^{-kL}) \qquad (3)$$

This corresponds to an albedo of 0.38 at $V = 0$ (desert) and 0.08 at maximum vegetation $V = 1$ (dense forest). Thus, vegetation feeds back into the atmosphere by modifying evapotranspiration and surface albedo through Eqs. 2 and 3.

In order to identify the relative importance of oceanic forcing as represented by SST, land surface, and vegetation processes, we performed a series of model experiments, starting from a run in which both land and vegetation were interactive. In this realistic case, designated AOLV, the atmosphere, ocean, land, and vegetation all contribute to variability. The monthly output from this run was then used to derive a vegetation climatology that has a seasonal cycle but does not change from year to year, which was used as a model boundary condition for the second run, designated AOL. The output of the run AOL was then used to derive a soil moisture climatology that was used to drive the third experiment, AO. In all these three runs, the coupled atmosphere–land-vegetation model is driven by the observed monthly SST from 1950 to 1998 (*22*). All three start from an initial condition taken from an interactive land-vegetation run forced by a climatological SST. The modeled annual rainfall over the Sahel from these experiments is shown in Fig. 1, B through D.

Compared to the observations in Fig. 1A, the AO run forced by interannually varying SST but with noninteractive soil moisture and vegetation (Fig. 1B) shows a weak interannual variation and a much weaker interdecadal signal, although a drying trend can be seen from the 1950s to the 1980s. The interactive soil moisture (Fig. 1C) appears to increase this interdecadal drying trend into the early 1990s. The simulated soil moisture shows a high degree of correlation with precipitation. The amplitude of interannual variation is also larger in general, in agreement with other studies (*23–25*).

Allowing vegetation feedback to the atmosphere in AOLV substantially enhances the decadal rainfall variability (Fig. 1D). The wet periods in the 1950s and the dry periods in the 1970s and the 1980s stand out and are more like observations of actual conditions. Compared to the noninteractive vegetation case, AOL, the interannual variability does not show enhancement. In some cases, the year-to-year change, such as from the dry 1987 to the relatively wet 1988, is actually reduced because the slowly responding vegetation is still low from the previous drought. This complicated lagged rela-

[1]Department of Atmospheric Sciences and Institute of Geophysics and Planetary Physics, University of California, Los Angeles, CA 90095–1565, USA. [2]NASA-Goddard Space Flight Center, Greenbelt, MD, 20771, USA.

*To whom correspondence should be addressed. E-mail: zeng@atmos.ucla.edu

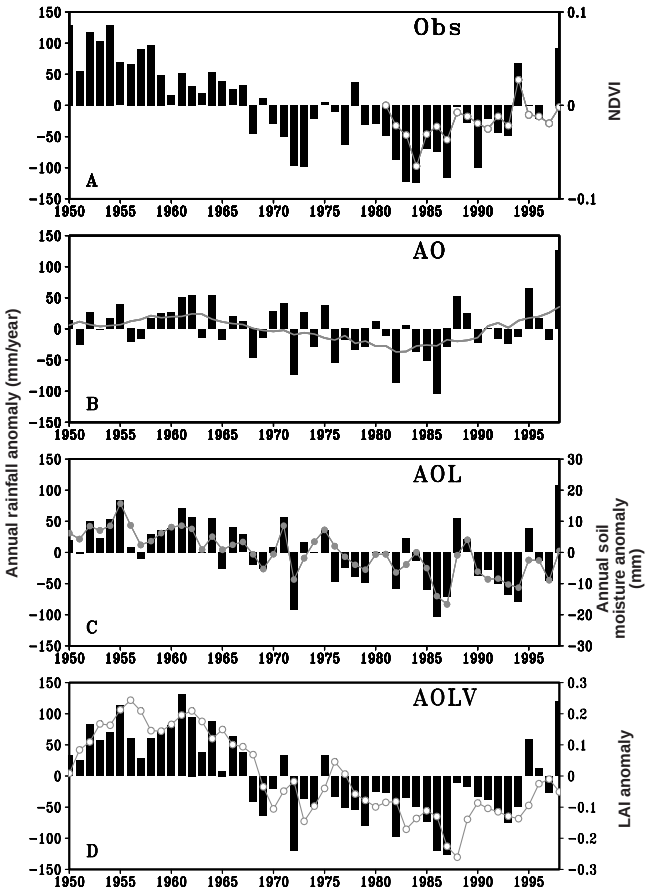

Fig. 1. Annual rainfall anomaly (vertical bars) over the West African Sahel (13N-20N, 15W-20E) from 1950 to 1998. (**A**) Observations from Hulme (*1*). (**B**) Model with noninteractive land surface hydrology (fixed soil moisture) and noninteractive vegetation (SST influence only, AO). Smoothed line is a 9-year running mean showing the low-frequency variation. (**C**) Model with interactive soil moisture but noninteractive vegetation (AOL). (**D**) Model with interactive soil moisture and vegetation (AOLV). Also plotted (as connected circles, labeled on the right) are (A) the normalized difference vegetation index (NDVI) (*31*), (C) the model simulated annual soil moisture anomaly, and (D) the model simulated LAI anomaly. All the anomalies are computed relative to the 1950–98 base period, except that the NDVI data is relative to 1981.

tionship between vegetation and precipitation is also seen in the observations (*26*), but our understanding of vegetation dynamics and the modeling tools available are not sufficient for a precise assessment of the reasons for this. Variation in rainfall drives a similar trend in vegetation through vegetation growth or loss (Fig. 1D). The vegetation lags slightly behind the rainfall, and its variation is also smoother, although these tendencies are not very strong, because the 1-year vegetation time scale used in the model runs is comparable to the time resolution of the plot.

To assess the internal climate variability in the model, additional nine-member ensemble runs have been conducted corresponding to each of the three cases above. The member runs in an ensemble differ only in their initial atmospheric and soil moisture conditions. We used the Sahel rainfall difference between the wet period 1950–67 and the dry period 1968–87 as an indicator of the amplitude of the interdecadal variation. Successive amplification of the decadal trend occurs with the inclusion of interactive soil moisture, especially vegetation (Fig. 2). However, even the AOLV ensemble still tends to underestimate the observed decadal trend, and the case shown in Fig. 1D is on the high side of the distribution. Furthermore, the scatter among the ensemble members also increases when additional feedbacks are included. Interactive vegetation increases the variance even though initial vegetation conditions are identical in these runs.

The interactive vegetation modifies the precipitation through a chain of positive feedback loops. For instance, decreased rainfall leads to less water availability and reduces vegetation, which in turn leads to higher surface albedo and reduced evapotranspiration. This weakens the large-scale atmospheric circulation by reducing the energy and water flux into the atmosphere column, thus further decreasing the local rainfall (*6, 10, 12, 27*).

The dynamic nature of the vegetation-climate interaction can be understood more precisely in a linear system by simplifying these feedback processes

$$\frac{dV'}{dt} = \frac{\alpha P' - V'}{\tau} \quad (4)$$

$$P' = \mu V' + F_0 e^{i\omega t} \quad (5)$$

Here V' and P' are perturbations in vegetation and precipitation, respectively, and they approximate the interannual and interdecadal anomalies shown above. The coefficients α and μ represent the strength of the local interaction between vegetation and the atmosphere. Equation 4 is a linearized version of the biomass equation (Eq. 1) because soil moisture is forced by precipitation. A similar expression was derived by Brovkin *et al*. (*28*). Equation 5 approximates the vegetation feedback to rainfall through changes in surface albedo in Eq. 3 and evapotranspiration in Eq. 2. Rainfall is sinusoidally forced at a frequency ω and an amplitude F_0, representing the SST-induced change in the large-scale atmospheric circulation.

The dependences on ω of the amplitude of P' and phase lag ϕ are shown in Fig. 3 (*29*). At low-frequency forcing ($\omega\tau \rightarrow 0$), vegetation has enough time to establish a near equilibrium with the precipitation, so the precipitation is enhanced by a factor of $1/(1 - \alpha\mu)$ with little phase lag. This explains the amplification of the interdecadal variation of rainfall shown in Fig. 1D. At high-frequency forcing ($\omega\tau \rightarrow \infty$), vegetation has little time to respond to the forcing because of its relatively long adjustment time; therefore, the precipitation variation is mostly a direct response to the forcing. At intermediate-frequency forcing, the amplitude is enhanced slightly, but the phase lag is at a maximum. This phase lag has significant consequences for the interannual variability. In 1988, for instance, the memory in vegetation of the previous drought years has delayed and reduced the otherwise strong wetting tendency resulting from SST-induced atmospheric circulation change (Fig. 1, C and D).

The modeled Sahel rainfall in AOLV shows a correlation with observations of 0.67, a significant improvement from a 0.44 correlation in AOL. However, the year-to-year comparison with the observations is not as satisfactory. When we decompose the Sahel rainfall time series into low-frequency (longer than 10 years) and high-frequency (shorter than 10 years) components, the correlation with the observation is only 0.1 at high frequency and 0.94 at low frequency for the AOLV run. The discrepancy in the interannual simulation, both in our model and in the GCMs (*4, 30*), may have a considerable contribution from chaotic atmospheric internal variability, for which model and observation can only be compared in a statistical sense.

Although we focus on natural climate variations involving vegetation change, this does not exclude any role anthropogenic land use change might play. It is possible that desertification might account for the remaining difference between the interactive vegetation run and observations in Fig. 2 on decadal time scales, but because the vegetation feedback acts to amplify Sahel rainfall variability that originates from SST variations, significant effects can occur with relatively small vegetation changes. The change of surface albedo (not shown in Fig. 1) on the interdecadal time scale is about 0.03 in the experiment with interactive vegetation (AOLV). This is a subtle change compared either to the albedo change values of 0.1 used in GCM desertification experiments (*6*) or to what could be estimated from satellite observations in earlier decades. Current satellite systems will be capable of measuring this level of variation for future decadal fluctuations. The present results suggest the importance of such measurements because of the role vegetation feedbacks can play in interannual and interdecadal climate variability in climatically sensitive zones such as the Sahel.

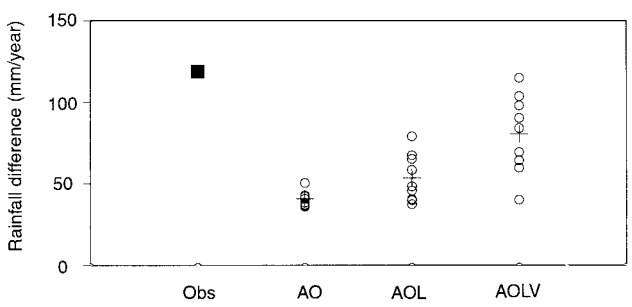

Fig. 2. Sahel rainfall difference between the period 1950–67 and the period 1968–87 for observations (solid square) and for three nine-member ensemble runs with and without interactive soil moisture and vegetation, similar to the ones in Fig. 1, B through D. Open circles denote individual ensemble members with different initial conditions and hence different chaotic internal variability. Crosshairs denote ensemble means.

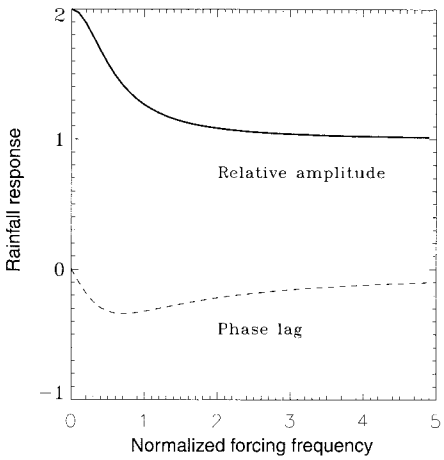

Fig. 3. Response of rainfall to a sinusoidal forcing in the idealized linear system (Eqs. 4 and 5), illustrating the dependence of vegetation feedback on forcing frequency. The response amplitude (P'/F_0, solid line) and phase lag (ϕ, in radians; dashed line) are plotted as a function of the forcing frequency $\omega\tau$ (normalized by the vegetation time scale τ).

References and Notes

1. Rainfall, based on the surface gauge data from M. Hulme [in *Global Precipitations and Climate Change*, M. Desbois and F. Desalmand, Eds. (NATO ASI Series, Springer-Verlag, Berlin, 1994), pp. 387–406], averaged over 15W-20E, 13N-20N, which approximately corresponds to the Sahel region as defined by S. E. Nicholson [in *Natural Climate Variability on Decade-to-Century Time Scales* (National Research Council, National Academy Press, Washington, DC, 1995), pp. 32–43].
2. C. K. Folland, T. N. Palmer, D. E. Parker, *Nature* **320**, 602 (1986).
3. D. P. Rowell, C. K. Folland, K. Maskell, M. N. Ward, *Q. J. R. Meteorol. Soc.* **121 A**, 669 (1995).
4. D. P. Rowell, *Q. J. R. Meteorol. Soc.* **122**, 1007 (1996).
5. F. H. M. Semazzi, B. Burns, N.-H. Lin, J.-K. Schemm, *J. Climate* **9**, 2480 (1996).
6. Y. Xue and J. Shukla, *J. Climate* **5**, 2232 (1993).
7. P. A. Dirmeyer and J. Shukla, *Q. J. R. Meteorol. Soc.* **122**, 451 (1996).
8. L. R. Holdridge, *Science* **105**, 367 (1947).
9. F. I. Woodward, *Climate and Plant Distribution* (Cambridge Univ. Press, Cambridge, 1987).
10. J. G. Charney, *Q. J. R. Meteorol. Soc.* **101**, 193 (1975).
11. J. Shukla and Y. Mintz, *Science* **215**, 1498 (1982).
12. R. E. Dickinson, in *Climate System Modeling*, K. E. Trenberth, Ed. (Cambridge Univ. Press, Cambridge, 1992), pp. 689–701.
13. M. Claussen, *Global Change Biol.* **4**, 549 (1998).
14. J. D. Neelin and N. Zeng, *J. Atmos. Sci.*, in press.
15. N. Zeng, J. D. Neelin, C. Chou, *J. Atmos. Sci.*, in press.
16. H. H. Shugart, *A Theory of Forest Dynamics: The Ecological Implications of Forest Succession Models* (Springer-Verlag, New York, 1984).
17. J.-J. Ji, *J. Biogeogr.* **22**, 445 (1995).
18. J. A. Foley *et al.*, *Global Biogeochem. Cycles* **10**, 603 (1996).
19. R. E. Dickinson, M. Shaikh, R. Bryant, L. Graumlich, *J. Climate* **11**, 2823 (1998).
20. P. J. Sellers *et al.*, *J. Climate* **9**, 676 (1996).
21. M. Verstraete, B. Pinty, R. E. Dickinson, *J. Geophys. Res.* **95**, 755 (1990).
22. R. W. Reynolds and T. M. Smith, *J. Climate* **7**, 929 (1994).
23. T. L. Delworth and S. Manabe, *Adv. Water Resour.* **16**, 3 (1993).
24. R. D. Koster and J. J. Suarez, *J. Geophys. Res.* **100**, 13775 (1995).
25. K.-M. Lau and W. Bua, *Clim. Dyn.* **14**, 759 (1998).
26. S. N. Goward and S. D. Prince, *J. Biogeogr.* **22**, 549 (1995).
27. N. Zeng and J. D. Neelin, *J. Climate* **12**, 857 (1999).
28. V. Brovkin, M. Claussen, V. Petoukhov, A. Ganopolski, *J. Geophys. Res.* **103**, 31613 (1998).

29. The solutions of Eqs. 4 and 5 for the oscillation amplitude and phase shift ϕ relative to the forcing for P' are

$$\left|\frac{P'}{F_0}\right|^2 = \frac{1+\omega^2\tau^2}{(1-\alpha\mu)^2+\omega^2\tau^2}$$

$$\tan(\phi) = -\frac{\alpha\mu\omega\tau}{1-\alpha\mu+\omega^2\tau^2}$$

For conditions on the approximations in Eq. 5, see (*27*). The coupling coefficients α and μ are positive and $\alpha\mu < 1$ so that the positive feedbacks do not become unstable. In Fig. 3, $\alpha\mu = 0.5$.

30. K. R. Sperber and T. N. Palmer, *J. Climate* **9**, 2727 (1996).
31. C. J. Tucker and S. E. Nicholson, *Ambic* **28**, 587 (1999).

32. Supported by NSF grant ATM-9521389, NOAA grant NA86GP0314, and a grant to N.Z. from the NASA IPA program. We thank two anonymous reviewers for their constructive comments, K. Hales for help with the rainfall data, M. Cisse for processing the normalized difference vegetation index data, and V. Nelson for editorial assistance.

14 July 1999; accepted 6 October 1999

The Gelation of CO_2: A Sustainable Route to the Creation of Microcellular Materials

C. Shi,[1] Z. Huang,[1] S. Kilic,[1] J. Xu,[1] R. M. Enick,[1] E. J. Beckman,[1]* A. J. Carr,[2] R. E. Melendez,[2] A. D. Hamilton[2]*

Compounds with strong thermodynamic affinity for carbon dioxide (CO_2) have been designed and synthesized that dissolve in CO_2, then associate to form gels. Upon removal of the CO_2, these gels produced free-standing foams with cells with an average diameter smaller than 1 micrometer and a bulk density reduction of 97 percent relative to the parent material.

Carbon dioxide is nonflammable, relatively nontoxic, and naturally abundant, and is consequently promoted as a sustainable solvent in chemical processing. Carbon dioxide's "green" properties have provided the driving force for development of a number of new applications, such as replacement of organic solvents in polymerization (*1*), as a medium for conducting hydrogenations and oxidations in the absence of transport limitations (*2*), as a solvent in biocatalysis (*3*), and as a raw material in synthesis (*4*). Many of these applications have been made possible by the relatively recent discovery that certain functional groups, subsequently denoted "CO_2-philic" (see below), enable miscibility of target compounds with CO_2 at moderate pressures (*5*). Development of CO_2-soluble surfactants, for example, permits CO_2-based emulsion polymerization and dry cleaning. The design and synthesis of CO_2-philic phosphine ligands has spawned a number of CO_2-soluble metal catalysts. By combining concepts in CO_2-philic design with an understanding of molecular assembly in solution, we have generated compounds that gel CO_2 at concentrations below 5 weight %. Creation of gels in CO_2 has allowed us to generate cellular polymers with a bulk density <5% of that of the parent polymer and cells <1 μm. Generation of gels, and more recently foams, using CO_2 thus provides a technically and environmentally satisfying solution to a material fabrication problem.

A one-step, CO_2-based route for generation of low bulk density, microcellular materials is of particular technical interest because these materials—organic analogs to silicate aerogels—have some intriguing applications (catalyst and separation supports, low-dielectric materials, insulation, tissue engineering scaffolds), and because current routes to organic and inorganic aerogels involve multiple process steps and large volumes of solvent. Commercial foaming processes using CO_2 are by contrast "greener," but they do not generate the combination of low bulk density and submicrometer pore size. These processes either add CO_2 to a polymer melt in an extruder or mix CO_2 with (polyurethane) precursor materials before polymerization. In either case, the pressure used is relatively low (30 to 100 atm), and thus the amount of CO_2 mixed with the polymer is usually <5 weight %. Foam with a very low bulk density (>95% density reduction relative to the parent polymer) is produced, but its cells can be as large as 1 mm (*6*). Research conducted during the 1980s and 1990s showed that high-pressure CO_2 (pressures up to 500 atm) can be used to swell thermoplastic polymers by as much as 30%, and that subsequent rapid depressurization produces a microcellular foam. Such methods readily produce foams with cells <2 μm, but density reductions rarely exceed 65% (*7*). There would be considerable utility in a single-step process by which one could generate organic, low-density, microcellular materials with a benign foaming medium such as CO_2.

As a means to generate low-density microcellular foam, we synthesized molecules that would dissolve in CO_2 under relatively moderate pressures, then associate in solution to form gels. Previous work has shown that gels can be created in traditional organic solvents through hydrogen bonding (*8*), association between ionic groups (*9*), or association between electron-donating and electron-accepting moieties (*10*). To form foams from such gels, it is necessary to preserve the supramolecular aggregates created in solution, both during and after solvent removal. Although it is possible to design molecules that aggregate in solution, for example through multipoint hydrogen-bond formation (*11*), only

[1]Department of Chemical and Petroleum Engineering, University of Pittsburgh, Pittsburgh, PA 15261, USA. [2]Department of Chemistry, Yale University, New Haven, CT 06520, USA.

*To whom correspondence should be addressed.